J Vis (2010) 13:213–220
DOI 10.1007/s12650-010-0029-y

REGULAR PAPER

**Sang Moon Kim · Seung Jae Yi · Hyun Dong Kim ·
Jong Wook Kim · Kyung Chun Kim**

# Dynamic analysis of bubble-driven liquid flows using time-resolved particle image velocimetry and proper orthogonal decomposition techniques

Received: 27 August 2009 / Accepted: 8 February 2010 / Published online: 14 March 2010

**Abstract** An experimental study to evaluate dynamic structures of flow motion and turbulence characteristics in bubble-driven water flow in a rectangular tank with a varying flow rate of compressed air is conducted. Liquid flow fields are measured by time-resolved particle image velocimetry (PIV) with fluorescent tracer particles to eliminate diffused reflections, and by an image intensifier to acquire enhanced clean particle images. By proper orthogonal decomposition (POD) analysis, the energy distributions of spatial and temporal modes are acquired. Time-averaged velocity and turbulent kinetic energy distributions are varied with the air flow rates. With increasing Reynolds number, bubble-induced turbulent motion becomes dominant rather than the recirculating flow near the side wall. Detailed spatial structures and the unsteady behavior of dominant dynamic modes associated with turbulent kinetic energy distributions are addressed.

**Keywords** Bubble-driven flow · Time-resolved particle image velocimetry · Proper orthogonal decomposition · Dynamic modes · Recirculation flow

## 1 Introduction

Bubble-driven flows are widely used in several industrial processes such as nuclear waste treatment, biochemical reactors, and steel making plants. In chemical engineering applications, mixing problems such as powder dispersion, solid blending, and gas dispersion into liquid are important issues because product quality and productivity depend highly on the mixing process (Luewisutthichat et al. 1997; Tirto et al. 2001; Tu and Trägårdh 2002).

Despite extensive applications of this basic flow phenomenon, the design of these systems has been mainly based on trial and empirical methods. Hence, a detail examination of mass, momentum, and energy transfer is essential for improving and optimizing the design of these industrial processes. However, the fluid dynamics complexity of turbulent, three-dimensional, two-phase flow combined with the coalescence and break-up of bubbles has not allowed researchers to devise comprehensive modeling procedures and establish design rules.

Bubbling mechanisms and induced mixing occur in a wide range of multi-phase flow systems. Driven by high volume moderate velocity gas injection into liquid baths, such flows are often chaotic and turbulent, and can feature a wide spectrum of interfacial length scales. The turbulence resulting from large bubble injection alters the characteristics of the heat and mass transfer in bubbling flows. For turbulent bubble-driven flows,

S. M. Kim · S. J. Yi · H. D. Kim · J. W. Kim · K. C. Kim (✉)
School of Mechanical Engineering, Pusan National University,
San 30, Jangjeon-dong Geumjeong-gu, Pusan 609-735, Republic of Korea
E-mail: kckim@pusan.ac.kr
Tel.: +82-51-5102324

little work has been done thus far, either experimentally or numerically. Durst et al. (1984, 1986) performed experimental studies on bubble-driven laminar flows by investigating liquid circulation and bubble's motion with a laser-Doppler system. It was reported that the liquid-phase circulation pattern is not sensitive to the actual shape of the void fraction profiles. Johansen et al. (1988) studied the fluid dynamics in bubble-stirred ladles by employing a laser-Doppler system to measure the axial and radial mean velocities and fluctuating velocities of the liquid phase. Air was supplied through a porous plug placed in the bottom wall of a cylindrical perspex model of a ladle. Recently, Montante et al. (2008) measured the turbulent gas–liquid flow and bubble size distribution in aerated stirred tanks using a two-phase PIV and a digital image processing method based on a threshold criterion. However, their experiments did not use a pure bubble-induced flow; rather, a Rushton turbine was included in the mixing tank.

Druault et al. developed a new POD application to recover the time information between two consecutive PIV time measurements based on time resolved PIV data of in-cylinder engine flows. By performing a POD over the full PIV velocity field snapshots, resulting POD coefficients were time interpolated so as to have a continuous space–time description of the turbulent flow field. He concluded that such interpolation procedure could be applied to any TRPIV turbulent flow fields (Druault et al. 2005).

Due to the lack of detailed experimental data for bubble-driven mixing flow, accurate velocity field data with appropriate time and space resolution is needed. Since the mixing characteristics in bubble-driven turbulent liquid flow is strongly governed by large-scale motions in the flow field, analysis of the large-scale dynamics is necessary to understand the mixing mechanism. In this study, we measured the entire flow field and analyzed the large-scale dynamic structures and turbulent characteristics in bubble-driven liquid flow in a rectangular tank using time-resolved PIV and POD techniques for the bubbling mixer.

## 2 Experimental methodology

Figure 1a shows a schematic of the experimental apparatus used in this study. A cubic tank (0.3 m length in each dimension) is made of transparent acrylic panels. Tab water was used as a working fluid, and compressed air was used to form the bubble stream. The height of the free surface is 0.15 m from the bottom wall. An air injection nozzle with a nozzle diameter $D_N$ of 5 mm was placed at the center of the bottom. The exit of the nozzle was 42 mm above the bottom wall. Compressed air was supplied to the nozzle through a regulator valve and a flow meter, so the flow rate of air could be precisely controlled by the flow meter. The flow rate of compressed air varied from 2 to 4 L/min at an air pressure of 0.5 MPa.

To reduce the diffused reflections originating from the bubbles and the nozzle, fluorescent polymer particles (Dantec Dynamics) were used. The maximum excitation wavelength of the particles is 550 nm, and the maximum emission wavelength is 590 nm. A laser beam 5 mm in diameter originating from a 532-nm diode CW laser passed through a spherical lens and a cylindrical lens, and turned into a 2-mm-thick sheet beam. The sheet beam irradiated the object plane through the transparent side wall. A ten bit high speed CMOS camera (1,280 × 1,024 pixels, pco.1200 hs, PCO) was used, and a 545-nm long-pass optical filter was mounted on the lens of the camera to eliminate diffused reflections. An image intensifier (UVI 507,

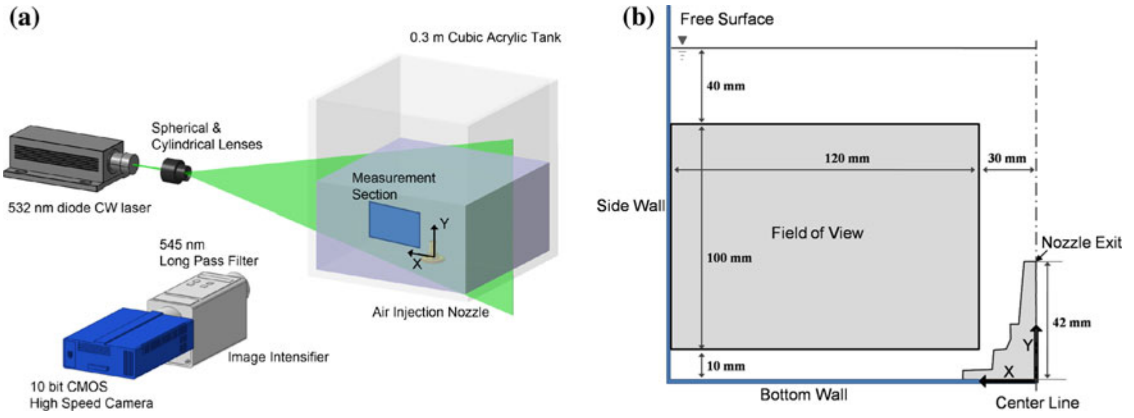

**Fig. 1** Schematic diagram of **a** experimental setup, **b** coordinate system and field-of-view

Invisible Vision Ltd.) was used to acquire enhanced clean particle images. Figure 1b shows the coordinate system defined and the field-of-view of the measurement section. The size of the field-of-view is 120 mm × 100 mm, and it was chosen to acquire the whole field of bubble-driven liquid flow just below the oscillating free surface and beside the bubble stream to avoid optical disturbances. A typical two-dimensional time-resolved PIV system was adopted. For each case, 1,000 images were acquired; the time interval between each image was 12.5 ms (80 frames/s), and the images were interrogated using the 2-frame cross-correlation technique. Interrogation windows were taken to be 48 × 48 pixels, respectively; the FFT window size was set to 64 × 64 pixels, and a 50% window overlap was adopted. False vectors in the raw vector fields were eliminated by using magnitude difference technique with 80% threshold and then interpolated with 3 × 3 Gaussian convolution.

## 3 Results and discussion

First, the mean diameters and mean velocity of bubbles were evaluated through the recorded flow visualization images for each case, and the bubble frequency from being detached from the nozzle exit was evaluated. Before PIV experiment, bubble diameter was estimated by recorded images in the high-speed camera under a halogen light illumination. Although the recorded image contains reflection and light diffusion, we can recognize the shape of bubble very clearly. Dimensionless parameters Reynolds and Eötvös number were calculated according to the following relations:

$$\text{Reynolds number} \quad Re = \frac{\text{inertial force}}{\text{viscous force}} = \frac{\rho_w V_B \cdot D_B}{\mu_w} \tag{1}$$

$$\text{Eötvös number} \quad Eo = \frac{\text{lift force}}{\text{surface tension force}} = \frac{g \Delta\rho D_B^2}{\sigma} \tag{2}$$

where $\rho_W$ is the density of the working fluid, $V_B$ is the mean rise velocity of the bubbles, $D_B$ is the mean diameter of bubbles calculated from images, $\mu_W$ is the absolute viscosity of the working fluid, $g$ is the acceleration of gravity, $\Delta\rho$ is the difference in density between the two phases, and $\sigma$ is the surface tension of the interface layer. The obtained flow parameters and dimensionless numbers are listed in Table 1. When the *Eo* and *Re* values of the three cases were plotted on the shape regime graph (Clift et al. 1978), all three cases are located in the regimes of "spherical cap" shape, and it is verified that the shape of the bubbles (cone shape) are similar to the spherical cap shape by visualization results.

Figure 2 shows the time-averaged velocity fields induced by bubbles for each case. A total of 999 instantaneous velocity fields were ensemble-averaged to obtain the mean velocity field. We note that there is upward flow driven by the bubble stream on the right half of the vector plots, and a counter-clockwise large vortical structure located at the upper left side. We observed inward flow at the right-bottom side of the view, induced by rising air bubbles.

When we compared the time-averaged velocity fields for each case, we observed the movement of the center of the vortical structure. As the flow rate of compressed air was increased, the center of the vortex moved outward and downward. In case I, the core location of the structure is $X/D_N = 22.5$ and $Y/D_N = 18.2$, but in case III, the core location of the structure moved to $X/D_N = 24.5$ and $Y/D_N = 15.5$. We believe that the increased flow of compressed air transferred more upward kinetic energy to the working fluid, the faster moving working fluid gained more inertial force, and this increased inertial force pushed the vortical structure outward and made it narrower. Therefore, the center of the structure moved outward. Then, due to the existence of a free surface and the side wall of the tank, the center of the structure moved downward.

An interesting result is found by comparing the amount of total kinetic energy of the mean velocity field. Using the velocity vectors in Fig. 2a–c, the estimated value of total mean kinetic energy for case I, II, and III are 0.069, 0.096, and 0.098 $m^2/s^2$, respectively. For the case II, the gas flow rate is 1.5 times higher than that

**Table 1** Parameters and dimensionless numbers

| Case | $Q$ (L/min) | $D_B$ (mm) | $V_B$ (m/s) | Bubble frequency (Hz) | *Re* | *Eo* |
|---|---|---|---|---|---|---|
| I | 2 | 21.8 | 0.31 | 13.5 | 6,744 | 64 |
| II | 3 | 24.0 | 0.39 | 14.0 | 9,341 | 77 |
| III | 4 | 25.0 | 0.53 | 15.0 | 13,223 | 84 |

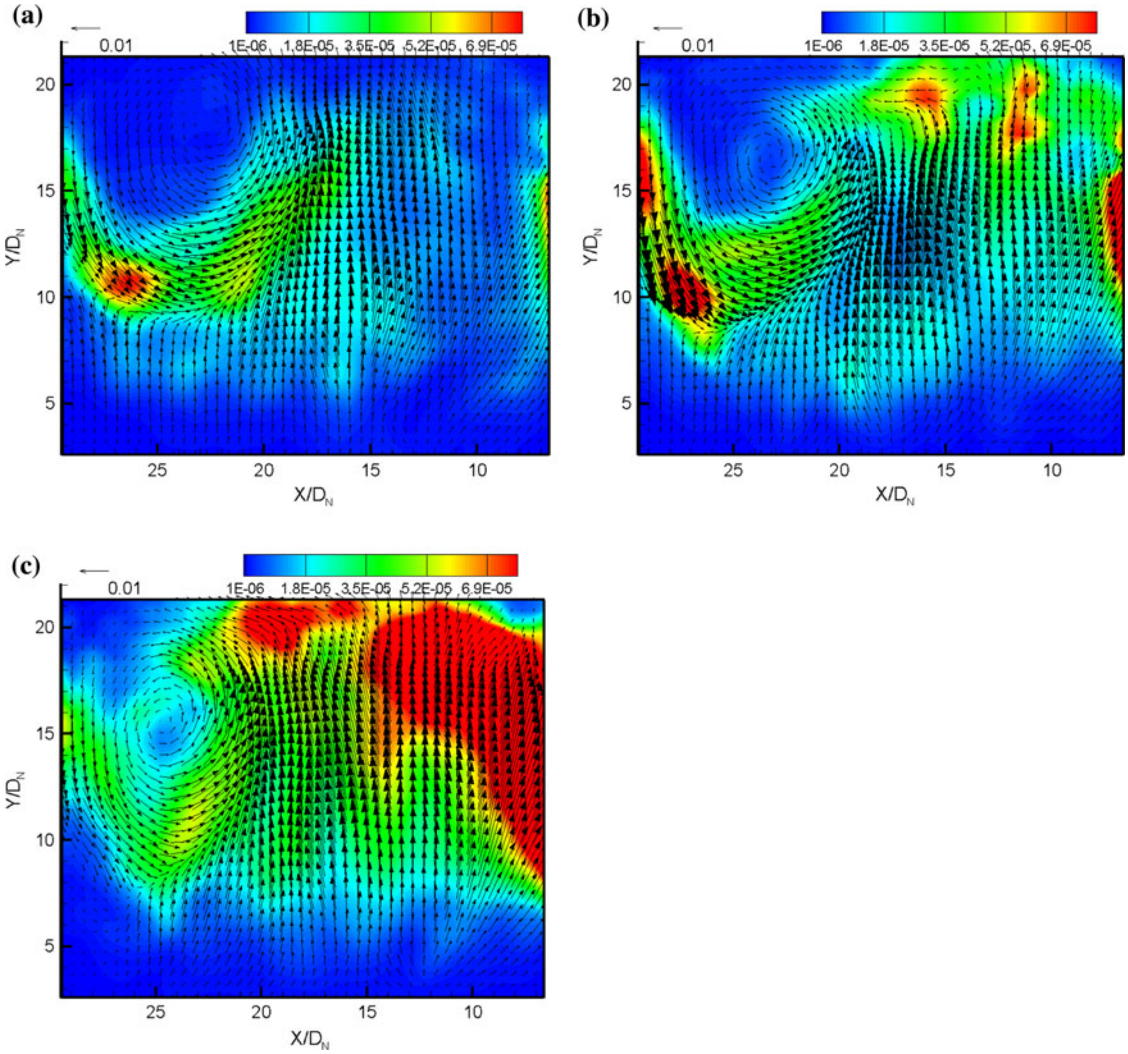

**Fig. 2** Mean velocity vector fields with turbulent kinetic energy contour for each case: **a** case I (2 L/min), **b** case II (3 L/min), and **c** case III (4 L/min)

of case I. For the same condition of gas pressure, the kinetic energy increased 1.39 times. However, the total kinetic energy of case III increased just 1.42 times compared to that of case I, although the flow rate increased two times. From this result, we conclude that energy transfer from the compressed air to the bubble-driven liquid flow was highly nonlinear, and that there must be an optimal condition for the efficient mixing process in a bubble-driven mixer.

To understand the mixing process, it is necessary to scrutinize not only the mean velocity field but also the turbulent characteristics associated with various flow conditions. The contour plots of Fig. 2 show the time-averaged turbulent kinetic energy field of each case. The summation of turbulent kinetic energy in the field of view for cases I–III is 0.022, 0.036, and 0.071 $m^2/s^2$, respectively. As the gas flow rate is increased, the turbulent kinetic energy level is increased dramatically over the measurement section. The overall kinetic energy in the measurement plane can be obtained by the addition of mean kinetic energy and turbulent kinetic energy. The resulting overall kinetic energy for cases I–III is 0.091, 0.132, and 0.170 $m^2/s^2$, respectively. The relative increases in overall kinetic energy in cases II and III are 1.45 times and 1.86 times higher compared to that in case I, respectively. These values are comparable to the relative gas flow rates in this experiment. The discrepancy is thought to be due to input energy loss to the vibration energy of the free surface.

In case I, the greatest turbulent kinetic energy is located at the recirculation zone, but in case III, it is located at the right side near the bubbling zone. In case II, the peak values of turbulent kinetic energy were found in the recirculating region near the free surface, and in the vicinity of the bubble rising region. We conclude that the dominant mechanism of turbulence generation strongly depends on the Reynolds number of the bubble-driven liquid flows. We observed from the visualization study that the bubbles moved with more vigorous agitation, and the fluctuation of the free surface became stronger as the gas flow rate increased.

Dynamic information of the flow field can be explained effectively using proper orthogonal decomposition (POD), from which the relative energy distribution is acquired. Using the POD technique as proposed by Lumley et al. (1993), the flow field can be decomposed into optimal orthogonal spatial modes and optimal orthogonal temporal modes. We executed a POD analysis using the method of snapshots and the instantaneous fluctuating velocity field from PIV data sets (Sirovich 1987). In our POD analysis, the eigenvalue represents the turbulent kinetic energy of each mode. The total number of modes is 999 since all the PIV data sets are used for POD analysis. The time-averaged mean flow field of case I has about 78% of the total kinetic energy, which is the dominant dynamic structure in the set of instantaneous velocity fields. It is shown that most of the turbulent kinetic energy is concentrated in the initial modes. As an example, in case I, the first 20 modes (the first 2% of the total number of modes) contain 83.6% of the total turbulent kinetic energy and 96.1% of the total kinetic energy, respectively.

Figure 3 demonstrates initial eigenmodes for a flow rate of 2 L/min, and the first mode (Fig. 3a) contains the greatest quantity of turbulent energy. We recognized that two counter-rotating vortices are inside the recirculating zone of the mean flow and large momentum region around the recirculating zone, as shown in Fig. 2a.

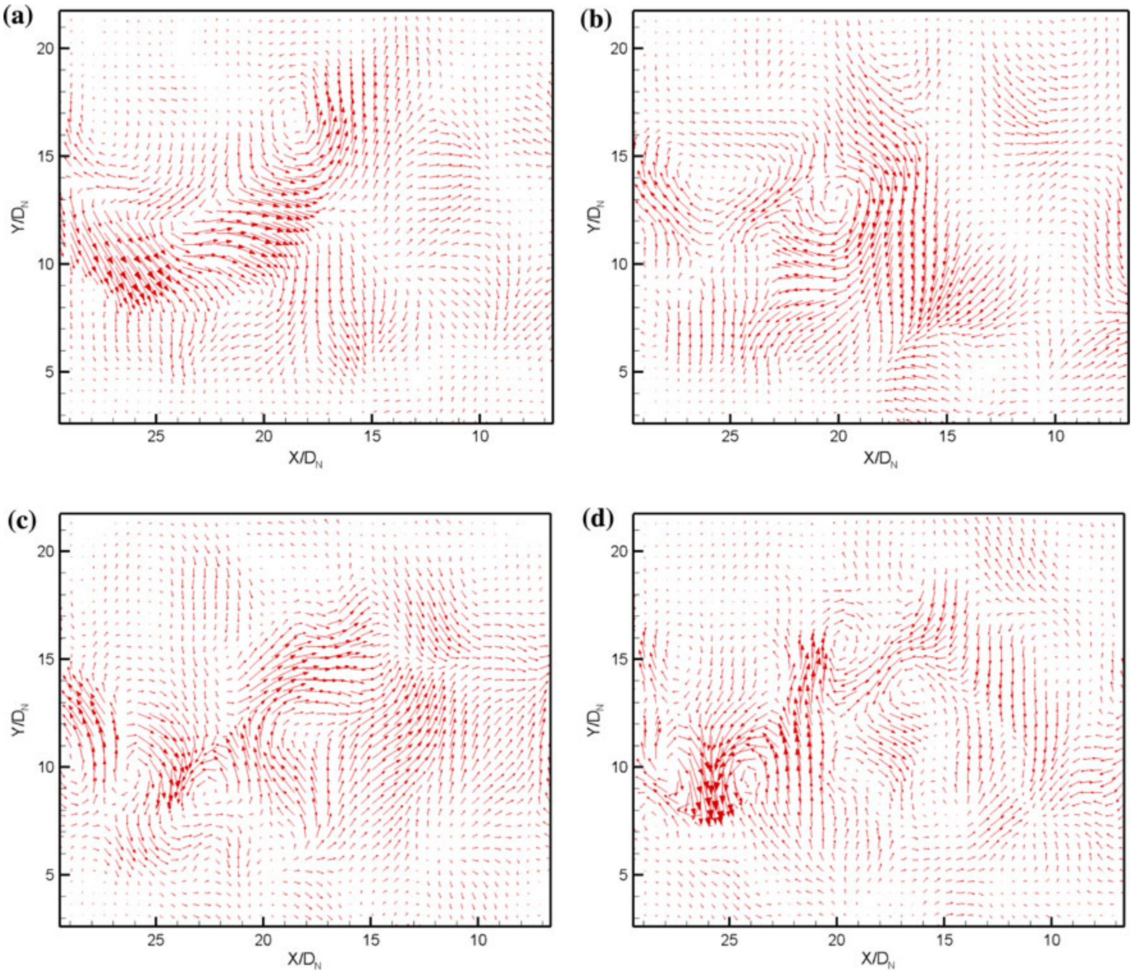

**Fig. 3** The first four eigenmodes of case I: **a** first spatial mode, **b** second spatial mode, **c** third spatial mode, and **d** fourth spatial mode

The second spatial mode (Fig. 3b) has three vortical structures related to the mean recirculating flow. Two vertically aligned counter-rotating vortices and a strong vortex induced the fluid to the bottom wall of the tank. Figure 3c, d depicts the third and fourth eigenmodes, which reveal that the large-scale structure became smaller through turbulent energy cascading. Higher modes appeared, as shown in Fig. 3c, d, but were not dominant in the overall flow field compared with Fig. 3a, b. However, those motions certainly contributed to turbulent mixing behavior. The third spatial mode depicts that four counter-rotating vortices aligned with the high turbulent kinetic energy region shown in Fig. 2a, and the fourth spatial mode has eight smaller vortices along the edge of the mean recirculating zone.

Figure 4 shows the first four eigenmodes when the air flow rate was 4 L/min. The spatial modes are quite different compared with those shown in Fig. 3. The first spatial mode (Fig. 4a) represents high momentum upward vertical flow due to the rising bubbles near the free surface, and the location coincides with the high turbulent kinetic energy region shown in Fig. 2c. A weak vertical flow pattern was also observed in the mean recirculating zone. The second spatial mode contains three different dynamics as shown in Fig. 4b. Upward vertical flow occurred near the free surface, and two counter-rotating vortices appeared in the region of mean recirculation and pushing flow from the bubble rising zone. As expected from the mean turbulent kinetic energy distribution of case III (Fig. 2c), turbulence production from the rising bubbles seems significant compared to case I. The third spatial mode showed only a pushing flow pattern from the rising bubbles. An interesting feature of the fourth spatial eigenmode is a suction flow mode due to the rising bubbles. We considered that that the low pressure region in the wake behind the moving bubbles entrained the nearby liquid. Unlike cases I, small-scale vortical motions did not appear in the first four spatial modes

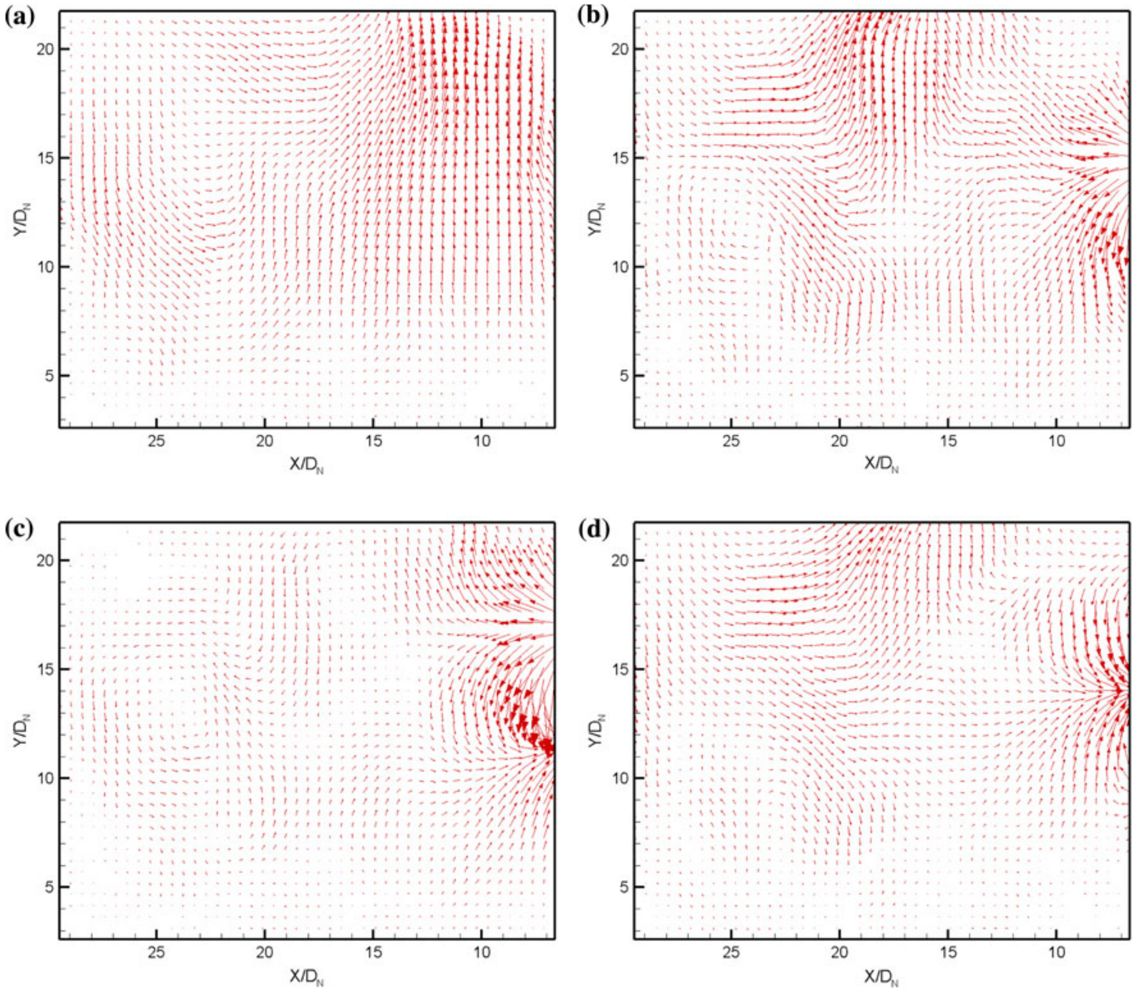

**Fig. 4** The first four eigenmodes of case III: **a** first spatial mode, **b** second spatial mode, **c** third spatial mode, and **d** fourth spatial mode

since the energy-containing eddies were dominated by the higher bubble rising velocity and free surface flow.

The temporal mode represents the time variation of energy containing in the corresponding spatial mode. We found there are many different time scales in the bubble driven flow such as eddy turnover time scale, bubble generating time scale, and surface wave-induced time scale. It can be conjectured that the temporal mode illustrates associated time scales with the corresponding spatial mode. The first temporal mode of case I shows very slow sinusoidal oscillation with a frequency of 0.08 Hz. The second temporal mode had the same frequency of oscillation, but there is a phase lag between the first and second modes (Fig. 5a). This kind of low frequency unsteadiness was observed for a low Reynolds number impinging jet in a confined wall (Kim et al. 2007). Since the bubble flow rising to the free surface is similar to the impinging jet to a normal wall, the low frequency oscillation can be explained as a kind of sloshing motion of the free surface or the bubble jet. The third and fourth temporal modes shown in Fig. 5a have the same frequency and phase, but the frequency is twice that of first and second mode modes. The first temporal mode (Fig. 5b) of case III oscillated with two distinct frequencies, 0.08 and 1.523 Hz. The low frequency might be attributed to the recirculating flow near the side wall, and its value is the same as that of the first mode in case I. We conjecture that the higher dominant frequency oscillation might be related to the vibration of the free surface, which interacts with the rising bubbles. The second temporal mode behavior was similar to the first temporal mode but contained much higher frequencies. Figure 5c, d illustrates the phase–space projections of the first and the second temporal modes for each case. The projection for case I (Fig. 5c) has an approximately circular shape with small oscillations along the circular shape, which means the time variations of the strength of the first and the second spatial modes are highly correlated with a 180° phase

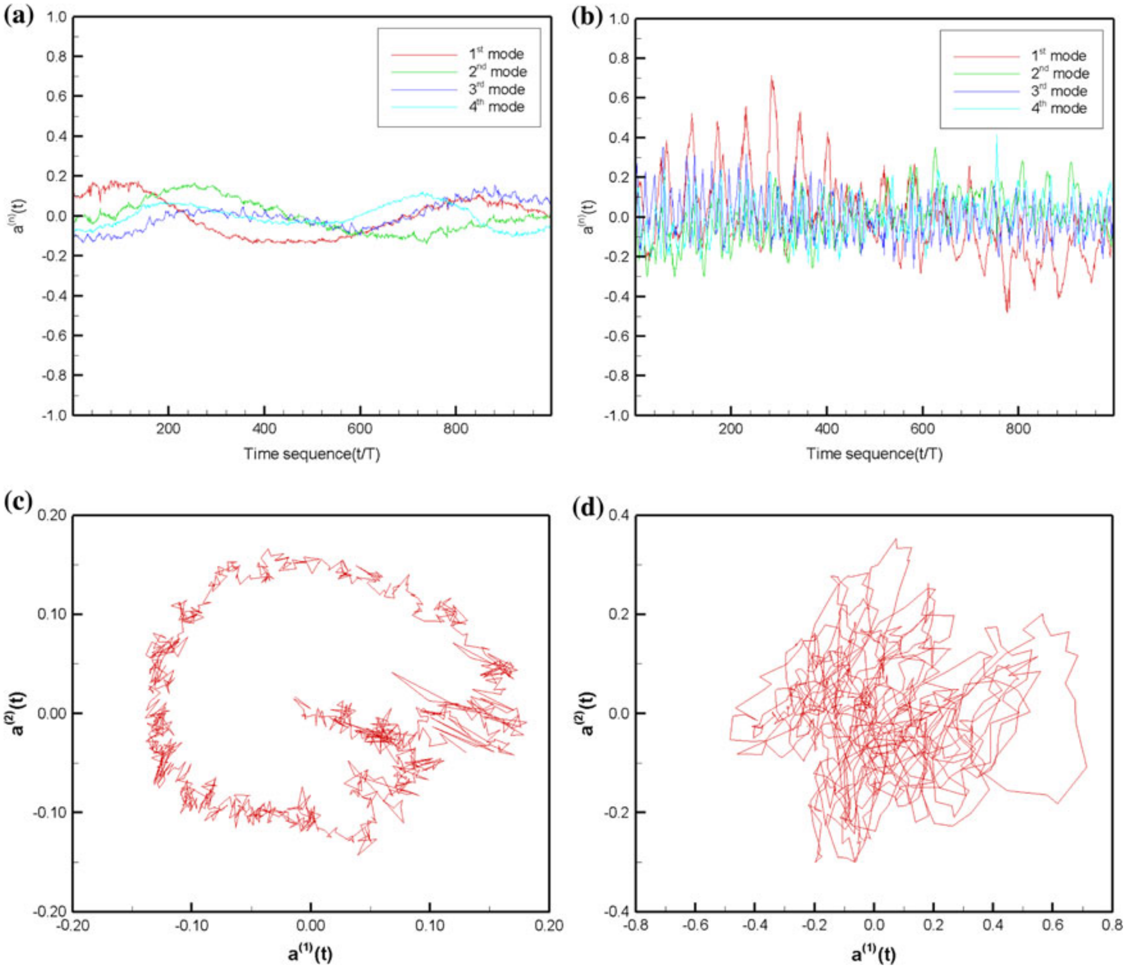

**Fig. 5** Temporal eigenmodes of **a** case I and **b** case III, and phase space projection of first temporal mode and second temporal mode of **c** case I and **d** case III

difference. The phase–space projection of case III shows a vividly random nature. It is clear that the two modes are uncorrelated since the first spatial mode is related to upward vertical flow and recirculating flow, whereas the second mode represents bubble-induced motion.

## 4 Conclusion

In order to investigate the dynamic characteristics of bubble-driven liquid flow with three different gas flow rates, an experimental study was conducted using the time-resolved PIV and POD techniques. Even though the time-averaged mean flow fields depicted similar flow patterns for all the cases, the dynamic characteristics of large-scale turbulent motions were significantly different with respect to the bubble Reynolds number. As the flow rates of compressed air were increased 1.5 and 2.0 times, the bubble rise velocities increased 1.3 and 1.7 times, and the magnitudes of the overall kinetic energy increased 1.45 and 1.86 times, respectively.

It was found that there are three dominant turbulence generation mechanisms: bubble induced turbulence, free surface oscillation, and recirculating vortex flow. In case I, most of the turbulent kinetic energy and the large-scale motions were concentrated in the mean recirculating zone. The first two temporal modes were highly correlated with each other, resulting in harmonic oscillation with the frequency of the turn-over time scale of the recirculating flow. As we increased the bubble Reynolds number, dominant turbulent motions were generated by the bubbles. The first four spatial modes obtained in case III vividly demonstrated outward and inward flow dynamics due to the unsteady bubble motions. The first and the second temporal modes in case III were uncorrelated, and showed a random nature in the phase diagram. Due to the presence of an oscillating free surface, energy transfer from the compressed air to the bubble-driven liquid flow had a distinct nonlinear manner. Therefore, more detailed studies should be conducted to investigate the interaction between the rising bubbles and the free surface.

**Acknowledgments** This research was supported by a Korea Science and Engineering Foundation (KOSEF) grant funded by the Korea government (MEST) (No. 2009-0080535). The second and third authors were supported by the second phase of the Brain Korea 21 Program in 2009.

## References

Clift R, Grace JR, Weber ME (1978) Bubbles, drops and particles. Academic press, New York

Druault P, Philippe Guibert P, Alizon F (2005) Use of proper orthogonal decomposition for time interpolation from PIV data: Application to the cycle-to-cycle variation analysis of in-cylinder engine flows. Exp Fluids 39:1009–1023

Durst F, Taylor AMKP, Whitelaw JH (1984) Experimental and numerical investigation of bubble-driven laminar flow in an axisymmetric vessel. Int J Multiphase Flow 10:557–569

Durst F, Schönung B, Selanger K, Winter M (1986) Bubble-driven liquid flows. J Fluid Mech 170:53–82

Johansen ST, Robertson DGC, Woje K, Engh TA (1988) Fluid dynamics in bubble stirred ladles: Part I. Experiments. Metallurgical Trans 19B:745–754

Kim KC, Min YU, Oh SJ, An NH, Seoudi B, Chun HH, Lee I (2007) Time-resolved PIV investigation on the unsteadiness of a low Reynolds number confined impinging jet. J Vis 10:367–380

Luewisutthichat W, Tsutsumi A, Yoshida K (1997) Chaotic hydrodynamics of continuous single-bubble flow systems. Chem Eng Sci 52:3685–3691

Lumley J, Holmes P, Berkooz G (1993) The proper orthogonal decomposition in the analysis of turbulent flows. Annu Rev Fluid Mech 25:539–575

Montante G, Horn D, Paglianti A (2008) Gas-liquid flow and bubble size distribution in stirred tanks. Chem Eng Sci 63:2107–2118

Sirovich L (1987) Turbulence and the dynamics of coherent structures. Part I: Coherent structures. Q Appl Math 45:561–571

Tirto P, Koichi T, Hideki T (2001) Effect of operating conditions on two-phase bubble formation behavior at single nozzle submerged in water. J Chem Eng 34:114–120

Tu X, Trägårdh C (2002) Methodology development for the analysis of velocity particle image velocimetry images of turbulent, bubbly gas-liquid flows. Meas Sci Technol 13:1079–1086